

PAPER • OPEN ACCESS

Study of a metal-halide perovskite CsPbBr₃ thin film deposited on a ¹⁰B layer for neutron detection



To cite this article: Jessica C Delgado *et al* 2024 *J. Phys. D: Appl. Phys.* **57** 055501

View the [article online](#) for updates and enhancements.

You may also like

- [Effects of electromagnetic and magnetic stresses on zebrafish samples](#)
V. Nassisi, L. Velardi, A. Mazzei et al.
- [Experimental analysis of a TEM plane transmission line for DNA studies at 900 MHz EM fields](#)
F Belloni, D Doria, A Lorusso et al.
- [The newly installed IBIL \(Ion Beam Induced Luminescence\) set-up at CEDAD-University of Salento: design and first applications on perovskite](#)
G. Quarta, A.P. Caricato, C. Provenzano et al.

Study of a metal-halide perovskite CsPbBr₃ thin film deposited on a ¹⁰B layer for neutron detection

Jessica C Delgado^{1,2,*} , Chiara Provenzano^{3,4,*}, Marcella Marra^{3,5}, Maurizio Martino^{3,5}, Anna Grazia Monteduro⁵, Sandra Moretto^{1,6}, Felix Pino¹, Matteo Polo^{7,8} , Gianluca Quarta^{3,5,9} and Anna Paola Caricato^{3,5}

¹ Department of Physics and Astronomy, University of Padova, Via Francesco Marzolo, 8, 35131 Padova, Italy

² Department of Physics and Earth Science, University of Ferrara, Via Giuseppe Saragat, 1, 44122 Ferrara, Italy

³ National Institute of Nuclear Physics, section of Lecce, Via Per Arnesano, 73100 Lecce, Italy

⁴ Department of Engineering of Innovation, University of Salento, Via Per Arnesano, 73100 Lecce, Italy

⁵ Department of Mathematics and Physics 'Ennio De Giorgi', University of Salento, Via Per Arnesano, 73100 Lecce, Italy

⁶ National Institute of Nuclear Physics, section of Padova, Via Francesco Marzolo, 8, 35131 Padova, Italy

⁷ Department of Industrial Engineering, University of Trento, via Sommarive 9, 38123 Povo, Trento, Italy

⁸ TIFPA-Trento Institute for Fundamental Physics and Applications, via Sommarive 14, 38123 Povo, Italy

⁹ CEDAD (Centro of Applied Physics, Dating, and Diagnostics) Department of Mathematics and Physics 'Ennio De Giorgi', University of Salento, Via Per Arnesano, 73100 Lecce, Italy

E-mail: jessicadelgadoalvarez@gmail.com and chiara.provenzano@unisalento.it

Received 18 July 2023, revised 18 September 2023

Accepted for publication 20 October 2023

Published 2 November 2023



CrossMark

Abstract

Metal halide perovskite materials have received significant attention in recent years due to their promising properties and potential applications, particularly their use as scintillator detectors, which is rapidly emerging due to their promising advantages as detectors, such as low costs, fast response, high quantum yield, strong absorption, scalability, flexibility, and emission wavelength tunability. Given the effectiveness of perovskites as α particle detectors and the potential of ¹⁰B as a neutron converter, in this paper a ¹⁰B converting layer was coupled with an all-inorganic lead halide perovskite (CsPbBr₃) layer aiming to create a thermal neutron detector. Specifically, a 1 μ m thin film of ¹⁰B and a 1 μ m thin layer of CsPbBr₃ were deposited on a suitable substrate using a laser ablation process. The fabricated detector was subjected to a comprehensive characterization, including structural, morphological, and detection properties. As output, the films exhibit macroscopically uniform behavior and good adhesion to the substrate. In terms of thermal neutron efficiency, an efficiency of $(7.9 \pm 0.3)\%$ was determined with respect to a commercial detector (EJ-426), which corresponds to an intrinsic efficiency of $(2.5 \pm 0.1)\%$. Also, Monte Carlo simulations were conducted, and the optimum value of the ¹⁰B layer thickness was found to be 2.5 μ m.

Keywords: perovskite, thermal neutron, detector

* Authors to whom any correspondence should be addressed.



Original Content from this work may be used under the terms of the [Creative Commons Attribution 4.0 licence](https://creativecommons.org/licenses/by/4.0/). Any further distribution of this work must maintain attribution to the author(s) and the title of the work, journal citation and DOI.

1. Introduction

Metal halide perovskites (MHPs) have recently attracted the attention of the materials science world and industrial research applications, thanks to their economic synthesis, adjustable band gaps, and optoelectronic properties [1]. In the last decade, the characteristics of perovskite materials have been discovered, and their huge potential as photodetectors [2, 3], light emitter devices [4], gas sensors [5] and radiation detectors [6–9] has been widely demonstrated. MHPs-based scintillators, specifically all-inorganic MHPs like CsPbBr₃, are emerging as very promising radiation detectors since they have demonstrated very high quantum yield [10], strong absorption ($Z_{\text{eff}} = 57.5$ [11]), flexibility [12, 13], emission wavelength tunability [14], and fast response (<10 ns [15]).

Perovskite-based α particles detectors [13, 16, 17], β particles [18], x-rays [19–21], and γ rays [22] have been investigated, and their performances are strictly related to their dimensionality (bulk, thin film, or nano-crystals) and deposition technique. In previous work performed by our group, the response of thin CsPbBr₃-based perovskite films, deposited by pulsed laser deposition (PLD), was studied under α particle (²⁴¹Am source) irradiation. A very fast response ($\tau \sim 5$ ns) was found, and a photoelectron yield of 40 % with respect to the CsI:Tl scintillator was obtained [23]. Also, it was analyzed the effects of post-growth aging, oxygen absorption, and annealing on the film properties, evaluating various annealing procedures carried out in different atmospheres and at different temperatures, and it was found to have a stable behavior over a long time, even when the films are exposed to high relative humidity conditions [24].

On the other hand, the detection of thermal neutrons (energy <0.5 eV; cadmium cut-off energy) plays a crucial role in various fields, including high-energy physics studies, fission and fusion research, nuclear power plants, homeland security, neutron imaging, large scientific research facilities, and nuclear medicine, among others [14, 25–31]. Neutron detection methods are generally based on the detection of secondary charged particles produced by the neutron capture reaction by ‘conversion’ elements, like ³He [32, 33], ⁶Li [34], and ¹⁰B [35], characterized by high cross-section for thermal neutron capture and high Q values [36]. In the nuclear reaction using ¹⁰B as conversion material (cross-section for thermal neutron capture reaction is 3840 barn [37]) two charged particles, one ⁷Li ion, and one α particle, are produced (see figure 1).

The detection of these secondary particles is performed through different methods and by making use of different devices, such as ionization chambers, Geiger–Muller counters, scintillation detectors, silicon detectors, etc [36]. Radiation detectors have been used for many years, but severe limitations in terms of radiation hardness, signal-to-noise ratio, spatial/time resolution, costs, and processability do exist. These limitations fuel continuous and intense research in the field of radiation detection, particularly in neutron detection. Novel design strategies in radiation detection

technology are recently moving towards thin, high-sensitivity, and high spatial/time-resolution solid-state devices, especially those characterized by low manufacturing costs and easy processability. In this respect, conventional semiconductors for high-energy detection have recently encountered strong potential competitors in the emerging class of perovskite materials.

In reference to thermal neutron detectors, our group conducted another study involving the deposition and characterization of a PLD-grown ¹⁰B film as a neutron converter. The film was coupled with a Silicon solid-state detector and exposed to a neutron flux emitted by an Am-Be neutron source at a rate of 2.2×10^6 s⁻¹. The results from both experimental measurements and simulations conducted using the GEANT4 toolkit showed excellent agreement, indicating a neutron detection efficiency of approximately 2% [35].

In previous studies, the combination of MHPs with ¹⁰B for thermal neutron detection has been explored and shown to offer significant advantages due to MHPs’ excellent optoelectronic properties and ¹⁰B’s high neutron capture capability [38–42]. In our work, we propose a bi-layer structure consisting of a ¹⁰B layer and a CsPbBr₃-based film, created using laser ablation (LA) deposition. Previous references, such as [39, 40], have demonstrated successful thermal neutron detectors based on halide perovskite nanocrystals, with thin-film CsPbBr₃-based diodes achieving intrinsic thermal neutron efficiencies of up to 4.3% at low bias voltages (-5 V). In our approach, we take advantage of the scintillation properties of the CsPbBr₃-based thin film, giving users the flexibility to choose an appropriate light sensor for their specific application needs. Our proposed detector achieves a similar intrinsic thermal neutron detection efficiency but gives the possibility to produce large-area detectors (25 cm²), significantly surpassing the small size of the CsPbBr₃-based diode (approximately 10^{-3} cm²). In figure 2 it can be seen a schematic view of the proposed detector. This technology is valuable for applications like thermal neutron imaging and detecting low-intensity thermal neutron fluxes, including special nuclear material detection, photo-fission, and neutron dosimetry. Furthermore, our thermal neutron detector offers the advantage of thin-film deposition on flexible substrates, enabling the creation of complex geometries that can optimize detection efficiency performance. Furthermore, in this work, the proposed detector is characterized in terms of structural, morphological, and thermal neutron detection performance.

2. Experimental methods

2.1. ¹⁰B thin film deposition and characterization

The deposition by LA of the ¹⁰B conversion layer has been performed in a stainless-steel vacuum chamber, evacuated down to 10^{-6} Pa thanks to a combined system of rotative and turbomolecular vacuum pumps. The film has been deposited by ablating a commercial 95% enriched ¹⁰B target

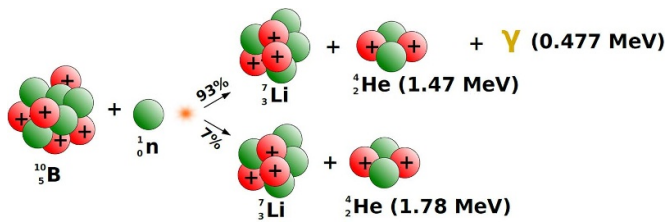


Figure 1. Scheme of the thermal neutron capture reaction on ^{10}B .

(American Elements Company, US) using the fundamental harmonic (1064 nm) of a Q-switched Continuum Powerlite-8010 Nd:YAG laser, with a pulse width of 7 ns. The laser beam has been focused on the ^{10}B target at an incidence angle of 45° , producing a spot area of about 4 mm^2 . During the ablation, the target has performed a combined motion of vertical spanning and rotation around its axis (1 Hz angular speed) in order to avoid the formation of craters because of multiple irradiations in the same area. The laser fluence has been set to 11 J cm^{-2} . The ablated material has been collected on a carbon fiber substrate, placed in front of the target at a distance of 40 mm, and with its axis shifted with respect to the plume axis (off-axis configuration). Finally, a $1\text{ }\mu\text{m}$ thick layer of ^{10}B has been deposited on the $50 \times 50\text{ mm}^2$ carbon fiber substrate at room temperature. The ^{10}B layer on the carbon fiber has a uniform circular area of about 30 mm in diameter.

It is important to highlight that the quality and properties of the deposited film were checked using the Rutherford backscattering (RBS) technique for density and composition. The morphology and structure of the film were also studied using SEM (Scanning Electron Microscopy), and XRD (x-ray Diffraction Spectroscopy) analysis. As an outcome, the film exhibits a macroscopically uniform behavior, free of flaws that could induce delamination and cracking, compromising its adhesion to the substrate [35].

2.2. CsPbBr_3 thin film deposition and characterization

The CsPbBr_3 perovskite film has been deposited on the ^{10}B film (which was previously deposited on a carbon fiber) via LA, using the experimental setup illustrated in figure 3. In this case, a KrF excimer laser (Lambda Physik), operating at the wavelength of $\lambda = 248\text{ nm}$, and a pulse width of 20 ns, has been focused and directed at 45° on the surface of a solid target of CsPbBr_3 , mechanically synthesized by mixing, for 15–20 min at room temperature, the powders of the precursors CsBr, and PbBr_2 (purchased from ChemPUR with purity of 99.9%) with a 1:1 M ratio. The pressed compound has been transferred to an oven for heat treatment (2 h at 400°C , followed by 2 h at 500°C). The resulting target has been mounted on a rotating, motorized stand. During the growth of the film, the substrate has been rotated at a frequency of 1.2 Hz. For the deposition of the film, the fluence and the laser frequency

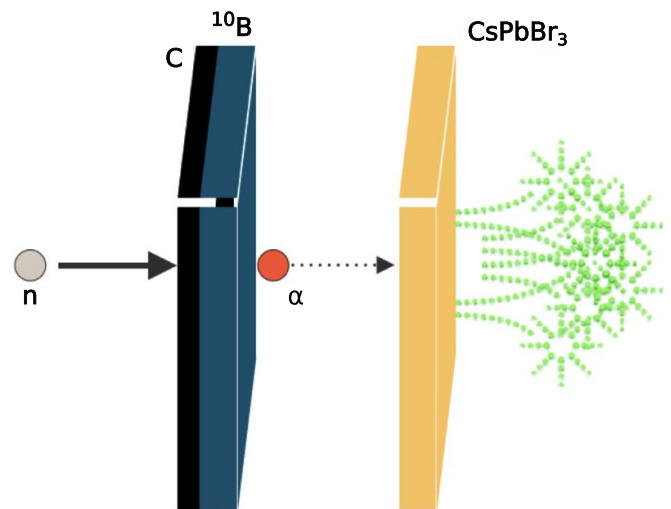


Figure 2. Schematic view of the bi-layer structure $\text{CsPbBr}_3/^{10}\text{B}$ (the gap between the ^{10}B , and the CsPbBr_3 layers is only for illustration purposes).

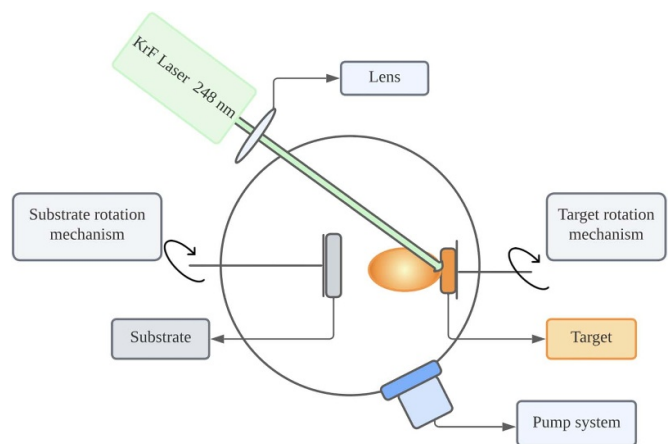


Figure 3. Pulsed laser deposition experimental setup.

have been set at 1 J cm^{-2} , and 2 Hz, respectively. Before starting the process, the vacuum chamber was evacuated down to a background pressure of 10^{-2} Pa , using a combined pumping system (rotative and turbomolecular). The ablated species have been collected on a carbon fiber/ ^{10}B substrate at room temperature, placed at a distance of 60 mm in front of the target, with an offset between the substrate axis and the target axis of approximately 4 mm.

For characterization purposes, a sample consisting only of the perovskite film deposited on the substrate was utilized. The sample underwent characterization using an XRD machine (Rigaku Company, Tokyo, Japan) in order to evaluate the crystalline properties of the film and its time evolution. The spectra were acquired using a $\text{Cu K}\alpha$ x-ray source with a wavelength of 1.54056 \AA . The instrument works with a voltage of 40 kV and an operating current of 40 mA. The

x-ray pattern was acquired over the angular range $2\theta = 10\text{--}50^\circ$. The film morphology and its time evolution have been analyzed by atomic force microscopy (AFM) with a Park XE-70 Instruments microscope (Park Systems, Suwon, Korea), operating in non-contact mode at room temperature and in the air environment. The optical and emission properties of the CsPbBr₃ film have been determined by UV-Vis and photoluminescence (PL) measurements [23]. Absorbance spectra were measured by a PerkinElmer Lambda 900 UV spectrophotometer (PerkinElmer Company, Waltham, MA) over a range of wavelengths of 200–800 nm and with a wavelength resolution of 3 nm. PL spectra were acquired by a solid-state continuous-wave (CW) laser delivering 100 mW at 405 nm with a diameter spot of 2 mm. The emission signal was collected in a back-scattering configuration by an optical fiber connected to a compact CCD (Oceanoptics), delivering a PL signal to the whole UV-Vis-NIR spectral window.

2.3. Experimental response of the bi-layer CsPbBr₃/¹⁰B detector

In order to explore the thermal neutron detection capabilities of the bi-layer CsPbBr₃/¹⁰B-based detector, its response has been studied using a moderated ²⁵²Cf source (2.0 MBq on February 15, 2014; at the moment of the measurement, the neutron emission rate was around $2.6 \times 10^4 \text{ s}^{-1}$). The fast neutrons were thermalized by placing 6 cm of polyethylene (PE) between the source and the detector (a source-detector distance of 10 cm). The CsPbBr₃/¹⁰B assembly was optically coupled to a photomultiplier (HAMAMATSU PMT model R6233) using clear and colorless coupling silicon grease. To supply the PMT bias voltage (+1250 V), a V6533 CAEN power supply module was employed. The signals coming from the PMT anode were digitized by a fast V1730 CAEN digitizer, which has an ADC resolution of 14 bits and a sampling rate of 500 MSamples s⁻¹. Modern digitizers are based on FPGA (Field Programmable Gate Array); in particular, in this work, the FPGA has an algorithm that provides for each triggered event, among others, the timestamp and the total (Q_{total}) integral of the signals. Besides, it is possible to record the signals as digitized waveforms in order to perform subsequent offline analysis. A CAEN VME-USB controller (V1718) has been used to manage the HV power supply unit from the computer. The V1730 digitizer has been connected and controlled from the computer through an optical fiber connection using the CAEN CONNET2 protocol and an A4818 CAEN USB 3.0 to CONET adapter. All parameters of the readout electronics and the data acquisition have been managed using the ABCD (Acquisition and Broadcast of Collected Data) software [43, 44], released as an open-source project (<https://github.com/ec-jrc/abcd>).

In order to verify and differentiate the thermal neutron events from other events that can interfere with the measurement, e.g. PMT dark current events and gamma-induced events on the PMT photocathode, a coincidence experiment was conducted first. The measurements have been performed

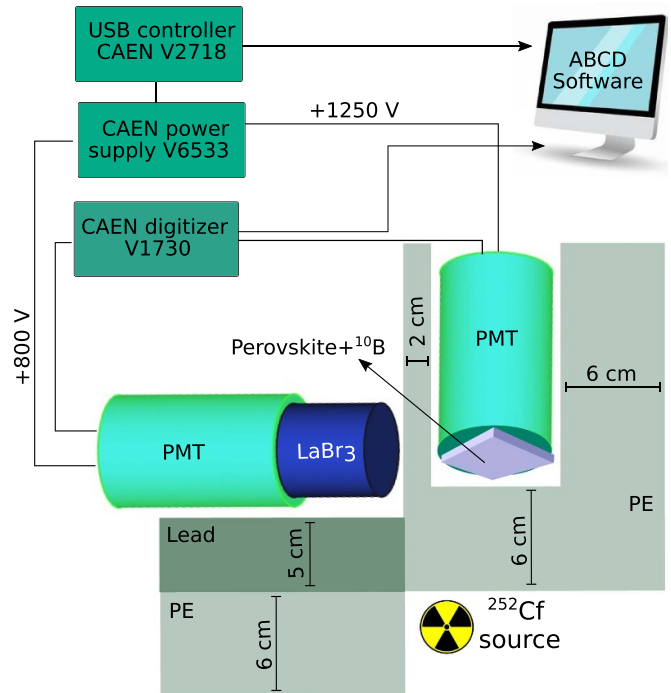


Figure 4. Experimental setup of the measurements performed in coincidence mode between the perovskite/¹⁰B based detector and the 2 × 2 LaBr₃:Ce detector, using a ²⁵²Cf source.

in coincidence between the perovskite/¹⁰B based detector and a 2 × 2 LaBr₃:Ce detector, using a ²⁵²Cf source. The recognition of the thermal neutron events on the CsPbBr₃/¹⁰B-based detector is done via the 0.477 MeV gamma-ray detection by the LaBr. This gamma-ray is emitted with 94% of probability right after a neutron capture reaction on ¹⁰B nucleus takes place (see the reaction scheme in figure 1). By selecting couples of the events based on the energy deposited on the LaBr and the almost co-occurrence of both events (time coincidence window set equal to 100 ns because several signal delays must be taken into account), it is possible to recognize and confirm the detection of thermal neutron events using the CsPbBr₃/¹⁰B based detector. In figure 4 there is an illustration of the experimental setup. Some centimeters of PE are needed for the thermalization of the fast neutrons, and a lead block is positioned next to the LaBr₃:Ce detector to shield the gamma rays coming from the source. For this run, the measurement time has been around 5 d (120 h).

After verifying and confirming the detection of the thermal neutrons with the CsPbBr₃/¹⁰B-based detector, a single-mode measurement was conducted, taking into account that this represents the most common configuration in which this assembly would be utilized. For the measurement, a ²⁵²Cf source was used. The measurement lasted around an hour. The fast neutrons coming from the source were moderated with a PE block of 6 cm in thickness placed in front of the source. A background measurement was made to produce a net spectrum by flipping the detector, i.e. the carbon fiber coupled to the PMT

and the perovskite layer watching the source. The efficiency of the detector was compared with that of a commercial detector (EJ-426 from Eljen Technology Texas-USA).

2.4. Monte Carlo modeling

Monte Carlo modeling was used to evaluate the detection performance of the proposed detector with the Geant4 v10.7 toolkit. The Monte Carlo simulation of the transport of radiation through the matter involves modeling the stochastic behavior of particles as they interact with the materials of the environment, consistently following the probabilities of various interaction processes, such as scattering, absorption, or the creation of secondary particles.

In this particular study, our focus was on simulating the interactions of thermal neutrons with the detector under investigation. These random events followed the respectively interaction probabilities, including neutron capture, which resulted in the generation of alpha particles. We meticulously traced the trajectories of these alpha particles as they interacted with the material, providing us with an estimation of the detector's response characteristics.

Specifically, these simulations played a crucial role in determining the optimal thickness of the ^{10}B layer. This determination holds immense importance since the detection efficiency is intricately linked to the thickness of the ^{10}B layer. A thicker layer increases the ^{10}B concentration, enhancing thermal neutron capture, but it also restricts the passage of alpha particles to the perovskite layer, where light emission occurs. Therefore, a delicate balance needed to be found in order to increase the detection efficiency of the detector.

In the simulations, the characteristics of the bi-layer $\text{CsPbBr}_3/^{10}\text{B}$ -based detector have been replicated in the G4VUserDetectorConstruction class, while the thickness of the ^{10}B layer has been modified (0.5, 1, 1.5, 2, 2.5, and 3 μm) in each simulation. The primary thermal neutrons were emitted from a square surface (with the same dimensions as the detector), and the primary source was positioned 10 cm away from the detector. In each simulation, 3×10^7 neutrons ($E_n = 0.025$ eV) were shot toward the face of the detector. The neutron transport has been managed with the high-precision neutron model for low-energy neutrons (<20 MeV) included on the QGSP_BERT_HP physics list. Using the G4Step, and G4Track classes (implemented on the G4UserSteppingAction class), it has been possible to track all the alpha, and ^7Li particles created after the neutron capture reaction on the boron layer; in particular, their kinematic information has been recorded, such as their energy deposition, direction, and interaction depth.

3. Results, and discussion

3.1. Compositional, structural and morphological characterization of the CsPbBr_3 film

The sample consisting only of the perovskite film deposited on the substrate was characterized by a defined absorption peak corresponding to the excitonic recombination close to the

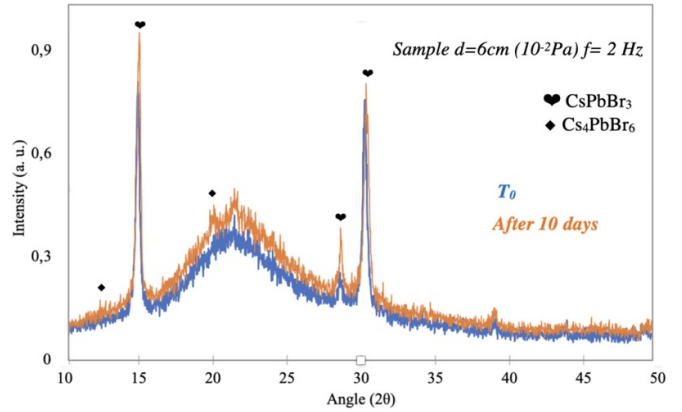


Figure 5. XRD spectra of the deposited CsPbBr_3 film over time.

edges of the direct band gap, but they did not present PL soon after the deposition because of a high density of surface traps. PL can be activated by post-deposition annealing treatments, which have the effects of increasing nanocrystalline domains, changing the CsPbBr_3 crystal phases from orthorhombic to cubic, and favoring oxygen adsorption. Similar effects can be obtained by prolonged exposure to the atmosphere [24]. Because of the role of the atmosphere on the emission properties of the film and considering that it has not been possible to thermally treat the film in this case due to the presence of the carbon fiber, the CsPbBr_3 film has been deposited using different growth conditions than those reported in [23]. A detailed discussion and motivation about the choice of the experimental parameters and their role in the film properties can be found in [23, 24, 45]. In particular, the film has been deposited at a low vacuum pressure (10^{-2} Pa), higher target-substrate distance (6 cm instead of 4 cm), and a lower repetition rate (2 Hz instead of 5 Hz). Twin films have been deposited on silica substrates too in order to characterize the perovskite film properties deposited under these conditions. The composition of the films has been estimated by the RBS technique, evidencing also, in this case, a Br deficiency ($\text{Cs}_{0.25}\text{Pb}_{0.22}\text{Br}_{0.53}$). The RBS analysis has also been used to calculate the thickness of the film, which differs by 7% moving from the center towards the edges of the sample [24], i.e. about $(1.00 \pm 0.07) \mu\text{m}$.

Under these deposition conditions, the XRD spectra evidence the predominance of the thermodynamically stable phase at room temperature, namely the orthorhombic phase CsPbBr_3 , with only a very faint hint of the presence of the cesium-rich phase Cs_4PbBr_6 [46, 47]. Although the main curve due to the amorphous phase could hide some characteristic peaks, the intensity and amplitude of the dominant diffraction lines at $2\theta = 15^\circ$, and indicates the dominance of the CsPbBr_3 phase with respect to the Cs-rich phase, as in figure 5. By analyzing the sample after two weeks, no substantial change has been observed other than the appearance of a faint peak at 20° associated with the Cs_4PbBr_6 cesium-rich phase (pdf reference card #73-2478). This is a very interesting aspect that deserves specific attention and a dedicated study since it is well known that deposited perovskite films

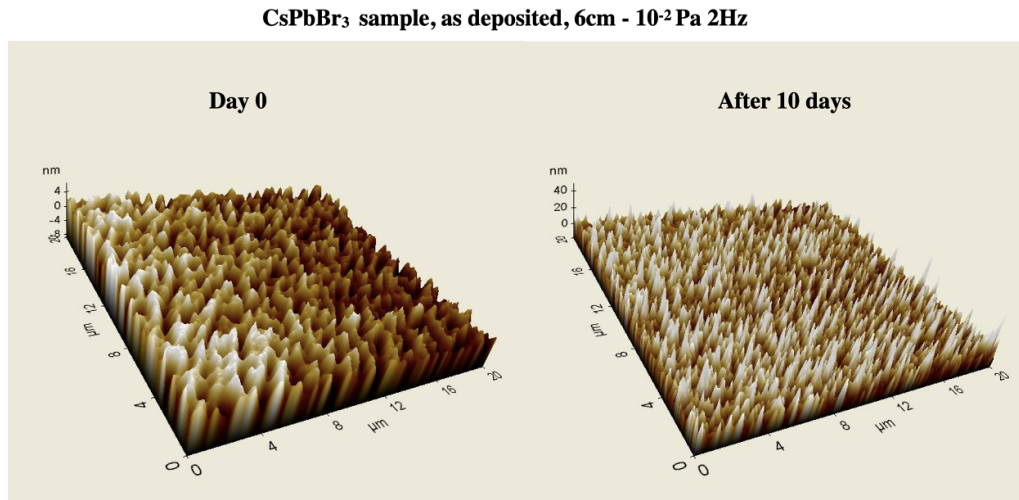


Figure 6. 3D topography acquired by AFM over time.

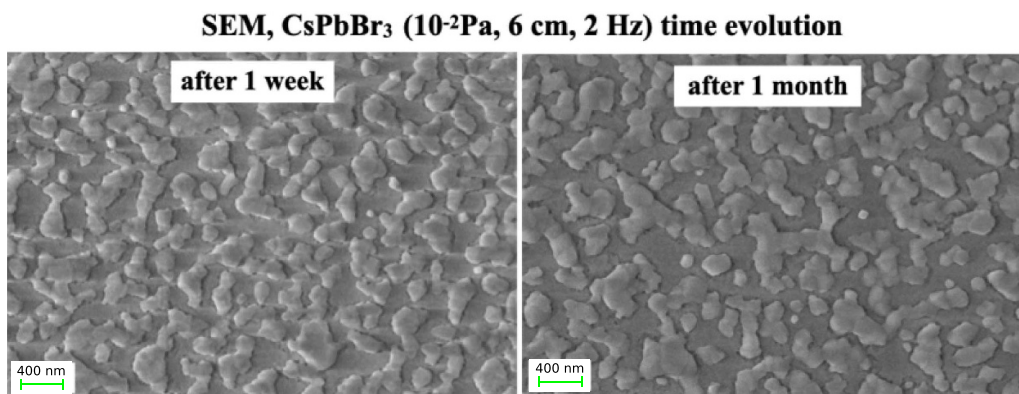


Figure 7. SEM images time evolution—one week and one month after the deposition.

present time evolution and degradation with time without any protective layer or further treatment [48, 49].

AFM analysis of the CsPbBr₃ film topography has been performed immediately after the deposition and after 10 d on 20 $\mu\text{m} \times 20 \mu\text{m}$ areas. The acquired images are reported in figure 6. Soon after the deposition, AFM measurements reveal a densely packed, pinhole-free background, while the foreground consists of columnar grains with sizes ranging from tens to about one hundred nanometers. The background fine-grained structure is the result of high-density nucleation seeds forming from the supersaturated deposition flux. As deposition progresses, grain growth and agglomeration lead to a bimodal distribution of grain sizes and the formation of large islands, which are facilitated by hyperthermal surface kinetics. As for surface roughness, the mean value increases over time (from 1.7 nm to 20.8 nm in 10 d), and the columnar structures become more visible and prominent, emerging above the background.

In figure 7, the evolution of a CsPbBr₃ sample through various SEM images acquired one week and one month after deposition can be observed. These images allow us to analyze

the structure of the foreground grains and observe their evolution over time. It is evident that during the aging process, the grains tend to coalesce, although with a slow kinetic, forming larger and more crystalline island structures, as confirmed by the previously discussed XRD spectra. The SEM images confirm the bimodal distribution of grain size observed in the AFM analysis, with the foreground consisting of columnar grains and the background composed of small, densely packed grains.

The LA perovskite films, deposited under high-pressure conditions, have demonstrated good stability regarding their optical properties too. In figure 8 it has been reported that the absorbance spectra of CsPbBr₃ films were obtained soon after the deposition and after 10 d. In both cases, two main absorption features are visible at about 310 nm and 516 nm, ascribed respectively to the Cs₄PbBr₆ phase [46, 50, 51], and to the typical absorption edge of CsPbBr₃ linked to the near excitonic recombination at the edges of the direct band gap [48, 49, 52, 53]. Only a slight increase of the peak at 310 nm has been observed, which is in agreement with XRD spectra and indicates a slow evolution of the Cs₄PbBr₆ phase. Details about the

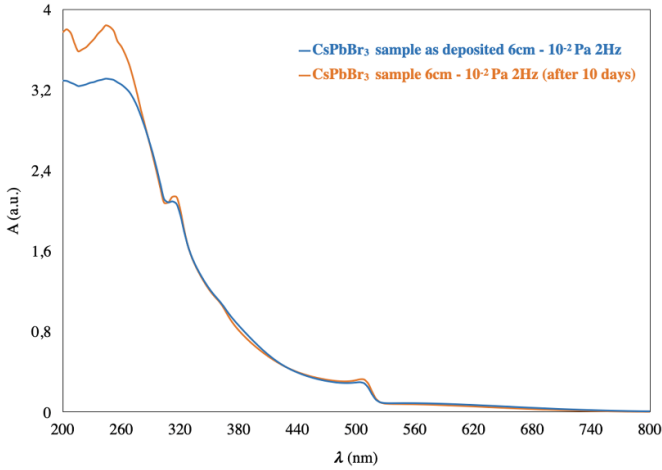


Figure 8. Absorbance spectra over time.

optical emission properties of the deposited films are reported in [23, 24, 45]. Consistent with what was reported in [23], the exposure to the atmosphere has been responsible for film luminescence under optical excitation due to oxygen uptake, which passively forms halide vacancies [54–56].

3.2. Neutron detection performance of the CsPbBr₃/¹⁰B based detector

3.2.1. Measurements in coincidence mode. The results obtained by doing the measurement in coincidence mode between the CsPbBr₃/¹⁰B based detector and the LaBr₃:Ce, using the ²⁵²Cf source, are displayed in figure 9. The complete set-up is given in figure 4. Specifically, figure 9(a) shows the 2D plot of the energy deposited by the gamma-rays in the LaBr (in MeV), against the light output (pulse-height) of the events registered by the CsPbBr₃/¹⁰B based detector. Inside the red square, it is indicated the cluster of events corresponding to the coincidences between the full-energy events at 0.477 MeV in the LaBr (gamma-ray emitted after the neutron capture reaction on ¹⁰B), and the events on the CsPbBr₃/¹⁰B based detector (time coincidence gate ~100 ns). Figure 9(b) shows the pulse-height (light output) spectrum of the CsPbBr₃/¹⁰B-based detector events inside the red square. Consequently, this spectrum certainly represents the thermal neutron events detected by the bi-layer CsPbBr₃/¹⁰B-based detector. Taking into account that the range of ⁷Li ions (of ~0.84 MeV) in boron is about 1.7 μm, most of the measured events are expected to be produced by the interaction of the alpha particles in the perovskite layer (the range of 1.5 MeV alpha particles in boron is 3.6 μm). The kinetic energy distribution of the alpha particles (as well as the energy deposited in the scintillator layer) follows an intricate distribution since they can be created at any location in the boron layer and must pass through a certain thickness of the boron layer (depending on the emission angle) before interacting with the perovskite. In section 3.3 more details are given.

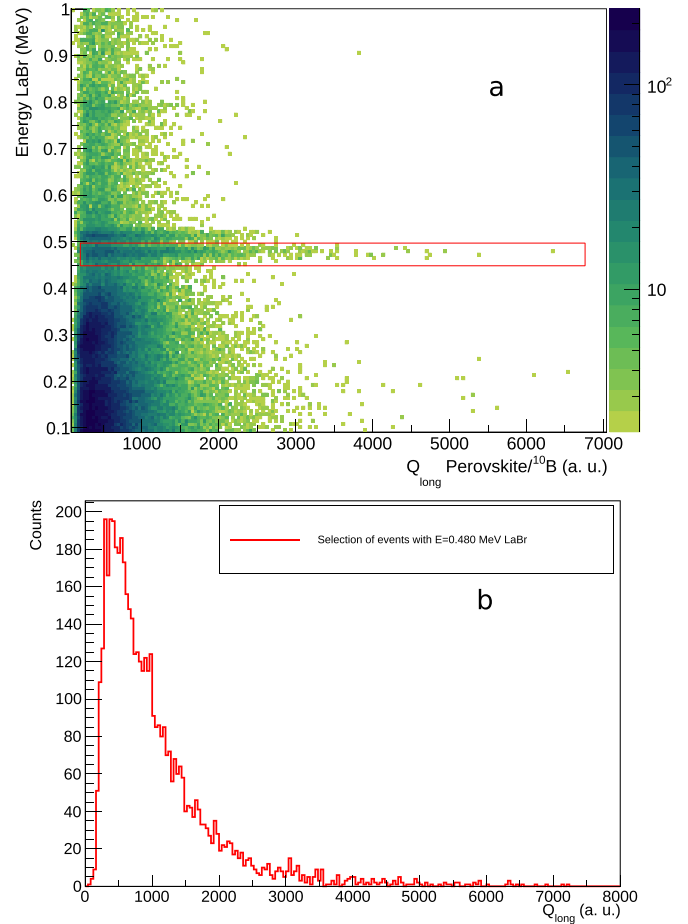


Figure 9. (a) 2D plot of the energy deposited in the LaBr₃:Ce against the light output of the event acquired by the bi-layer perovskite/¹⁰B based detector. (b) The light output spectrum of the perovskite/¹⁰B-based detector events inside the red square.

3.2.2. Measurements in single mode. The net spectrum is given in figure 10. As can be seen, the shape of the single-mode spectrum is very similar to the one obtained in coincidence mode. The net counting rate (integral of the mentioned spectrum) observed is (3.8 ± 0.1) cps. From the background measurement, it can be concluded that most of the background events correspond to gamma rays that interact directly with the photocathode of the PMT, taking into account that the intensity of gamma rays emitted by a ²⁵²Cf source is around 2.3 times that of neutron emission.

The efficiency of the studied detector with respect to a commercial detector (EJ-426) is around $(7.9 \pm 0.3)\%$. The measurement with the EJ-426 was performed in the same experimental condition of the one used with proposed detector. Taking into account that the manufacture reports an intrinsic efficiency of 31% for the EJ-426 detector, it is possible to conclude that the absolute efficiency of the bi-layer CsPbBr₃/¹⁰B based detector is around $(2.45 \pm 0.10)\%$.

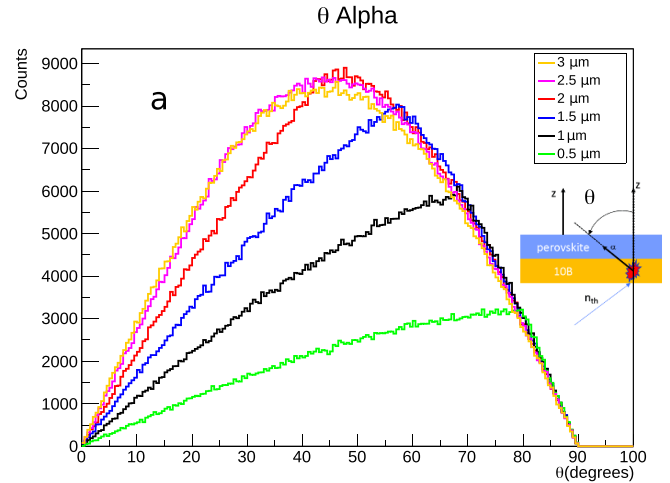
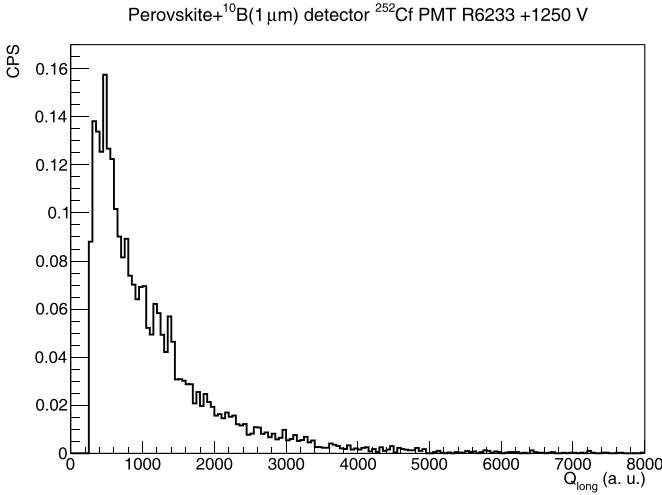


Figure 10. Net light output spectrum in single mode of the bi-layer perovskite/¹⁰B based detector, using a moderated ²⁵²Cf source.

3.3. Monte Carlo simulations

In the simulations, all the alpha particles that reached the perovskite layer and deposited some energy were tracked, and in consequence, the energy deposited and the initial output angle θ (with respect to the normal of the perovskite layer) were recorded for each event. In figures 11(a) and (b) the distribution of the initial output angle and the spectrum of the energy deposited by the alpha particles as a function of the ¹⁰B layer thickness can be seen. An effect of the solid angle and the thickness of the conversion layer can explain the shape of the distribution of the event output angle (see figure 11(a)). Also, alpha particles that were emitted at a too-inclined angle with respect to the normal (Z-axis) have lower probabilities of reaching the perovskite layer because, as the particle’s path in the converter is longer, the alpha particle loses more of its energy until it is stopped. In the energy spectra given in figure 11(b), the two full-energy peaks corresponding to the two branches of the neutron capture reaction on ¹⁰B, i.e. alpha particles of 1.47 MeV (94%), and 1.78 MeV (6%), can be seen for all the converter thicknesses. As the ¹⁰B layer thickness increases, the detection efficiency also grows, up to 2.5–3 μm . This result can be deduced by looking at the areas under the energy spectra. In fact, in figure 11(c) the total number of alpha particles (equivalent to the number of thermal neutrons detected) that reach the CsPbBr₃ layer as a function of the ¹⁰B layer thickness is shown. The counts have been normalized to the number of primary neutrons (3×10^7). The maximum value is obtained for a thickness of 2.5 μm , which can be used to guide future research. Nonetheless, based on the results, the choice of 1 μm as the converter’s thickness represents a good average option in terms of effort required to increase the ¹⁰B thickness and detection efficiency obtained. Also, in figure 11(c) it can be seen the absolute efficiency obtained experimentally of the detector under study (see section 3.2.2), a value which is higher to the simulation result with a discrepancy of 20%, a difference that could be due

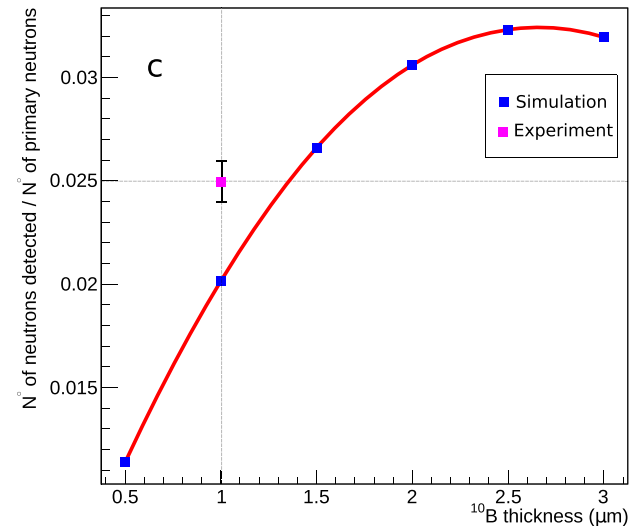
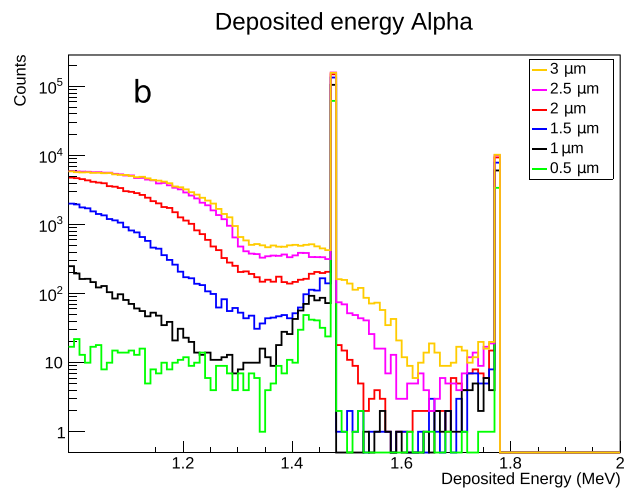


Figure 11. (a) Output initial angle distribution, (b) energy deposition, and (c) normalized number of detected alpha particles for different thicknesses of the ¹⁰B layer.

to the assumption that the EJ-426’s efficiency is 31%, and it could have decreased due to aging, degradation, and use of the detector.

4. Conclusion

This paper investigates the possibility of developing a thermal neutron detector by combining a high-performance scintillation material, consisting of a thin film of CsPbBr₃ perovskite, with a neutron conversion layer, specifically a thin film of ¹⁰B. The detector was constructed by depositing a ¹⁰B film and a perovskite layer onto a carbon fiber substrate (50 × 50 mm²) using LA. The process resulted in a uniform ¹⁰B film with a thickness of 1 μm on the substrate. On top of this ¹⁰B film, a 1 μm layer of CsPbBr₃ perovskite was deposited. In previous research [35], the compositional, structural, and morphological characterization of the ¹⁰B film has already been conducted. In the present work, a comprehensive characterization of the perovskite film is performed using RBS spectroscopy, SEM, and XRD techniques. The results of the characterization indicate that both layers, the ¹⁰B, and the perovskite films, exhibit good adherence to the substrate. Additionally, the films demonstrate a homogeneous and stable consistency without any signs of delamination or cracking, essential physical properties needed to make a detector.

The proficiency of the CsPbBr₃/¹⁰B-based detector in detecting thermal neutrons was investigated. The study involved single and coincidence mode measurements using a moderated neutron-gamma source (²⁵²Cf). The results from both setups exhibited excellent agreement. The thermal neutron efficiency of the detector, compared to a commercial detector (EJ-426), was determined to be (7.9 ± 0.3)%, which corresponds to an intrinsic efficiency of (2.45 ± 0.10)%. Monte Carlo simulations were performed to optimize the thickness of the ¹⁰B layer. The simulations revealed that the highest performance is obtained with a thickness of 2.5 μm, while a thickness of 1 μm results in an efficiency approximately 40% lower than the optimal value. Therefore, future studies may benefit from increasing the thickness of the ¹⁰B layer to 2.5 μm in order to enhance the efficiency of the detector.

Data availability statement

The data that support the findings of this study are available upon request from the authors.

Conflict of Interest

The authors have no conflicts of interest to disclose.

ORCID iDs

Jessica C Delgado  <https://orcid.org/0000-0002-1017-1554>
Matteo Polo  <https://orcid.org/0000-0003-4269-973X>

References

- [1] Jena A K, Kulkarni A and Miyasaka T 2019 *Chem. Rev.* **119** 3036–103
- [2] Horváth E, Spina M, Szekrényes Z, Kamarás K, Gaal R, Gachet D and Forró L 2014 *Nano Lett.* **14** 6761–6
- [3] Andričević P, Kollár M, Mettan X, Náfrádi B, Sienkiewicz A, Fejes D, Hernádi K, Forró L and Horváth E 2017 *J. Phys. Chem. C* **121** 13549–56
- [4] Andričević P, Mettan X, Kollár M, Náfrádi B, Sienkiewicz A, Garma T, Rossi L, Forró L and Horváth E 2019 *ACS Photonics* **6** 967–75
- [5] Mantulnikovs K, Glushkova A, Matus P, Čirić L, Kollár M, Forró L, Horváth E and Sienkiewicz A 2018 *ACS Photonics* **5** 1476–85
- [6] Yakunin S et al 2015 *Nat. Photon.* **9** 444–9
- [7] Mescher H et al 2020 *ACS Appl. Mater. Interfaces* **12** 15774–84
- [8] Huang K, Yang K, Li H, Zheng S, Wang J, Guo H, Peng Y, Zhong X and Yang J 2020 *ACS Appl. Energy Mater.* **3** 7318–24
- [9] Song Z, Zhao C, Liao F and Zhao Y 2019 *ACS Appl. Mater. Interfaces* **11** 32969–77
- [10] Xu Q, Wang J, Shao W, Ouyang X, Wang X, Zhang X, Guo Y and Ouyang X 2020 *Nanoscale* **12** 9727–32
- [11] Liu F, Wu R, Wei J, Nie W, Mohite A D, Brovelli S, Manna L and Li H 2022 *ACS Energy Lett.* **7** 1066–85
- [12] Wei H and Huang J 2019 *Nat. Commun.* **10** 1066
- [13] Gandini M et al 2020 *Nat. Nanotechnol.* **15** 462–8
- [14] Chen Q et al 2018 *Nature* **561** 88–93
- [15] Zhang Y et al 2019 *ACS Nano* **13** 2520–5
- [16] Xie A et al 2020 *Commun. Mater.* **1** 37
- [17] Mykhaylyk V B, Kraus H, Kapustianyk V, Kim H J, Mercere P, Rudko M, Da Silva P, Antonyak O and Dendebera M 2020 *Sci. Rep.* **10** 8601
- [18] Yu D, Wang P, Cao F, Gu Y, Liu J, Han Z, Huang B, Zou Y, Xu X and Zeng H 2020 *Nat. Commun.* **11** 3395
- [19] Yuan W, Niu G, Xian Y, Wu H, Wang H, Yin H, Liu P, Li W and Fan J 2019 *Adv. Funct. Mater.* **29** 1900234
- [20] Heo J H, Shin D H, Park J K, Kim D H, Lee S J and Im S H 2018 *Adv. Mater.* **30** 1801743
- [21] Maddalena F et al 2021 *J. Phys. Chem. C* **125** 14082–8
- [22] Náfrádi G, Horváth E, Kollár M, Horváth A, Andričević P, Sienkiewicz A, Forró L and Náfrádi B 2020 *Energy Convers. Manage.* **205** 112423
- [23] Caricato A P et al 2022 *Front. Phys.* **10** 957991
- [24] Cesaria M, Quarta G, Guascito M R, Mazzeo M, Marra M, Provenzano C, Aziz M R, Martino M, Calcagnile L and Caricato A P 2022 *Appl. Phys. A* **128** 950
- [25] Akkerman Q A, Gandini M, Di Stasio F, Rastogi P, Palazon F, Bertoni G, Ball J M, Prato M, Petrozza A and Manna L 2016 *Nat Energy* **2** 1–7
- [26] Lin K et al 2018 *Nature* **562** 245–8
- [27] Rainò G, Becker M A, Bodnarchuk M I, Mahrt R F, Kovalenko M V and Stöferle T 2018 *Nature* **563** 671–5
- [28] Ullah S, Wang J, Yang P, Liu L, Yang S E, Xia T, Guo H and Chen Y 2021 *Mater. Adv.* **2** 646–83
- [29] Tong G, Ono L K and Qi Y 2020 *Energy Technol.* **8** 1900961
- [30] Yin Y, Ali M U, Liu M, Miao J, Peng W, Li D, Chen S, Lee C and Meng H 2019 *Small* **15** 1901954
- [31] Bruzzi M, Talamonti C, Calisi N, Caporali S and Vinattieri A 2019 *APL Mater.* **7** 051101
- [32] Hurd A J and Kouzes R T 2014 *Eur. Phys. J. Plus* **129** 236
- [33] Kouzes R T, Lintereur A T and Siciliano E R 2015 *Nucl. Instrum. Methods Phys. Res. A* **784** 172–5
- [34] Finocchiaro P, Cosentino L, Lo Meo S, Nolte R and Radeck D 2018 *Nucl. Instrum. Methods Phys. Res. A* **885** 86–90
- [35] Caricato A P et al 2022 *Eur. Phys. J. Plus* **137** 431
- [36] Knoll G F 1989 *Radiation Detection and Measurement* 2nd edn (Wiley)

- [37] Brown D, Chadwick M, Capote R, Kahler A, Trkov A and Herman E A 2018 *Nucl. Data Sheets* **148** 1–142
- [38] Caraveo-Frescas J A, Reyes-Banda M G, Fernandez-Izquierdo L and Quevedo-Lopez M A 2022 *Adv. Mater. Technol.* **7** 2100956
- [39] Fernandez-Izquierdo L, Reyes-Banda M G, Mathew X, Chavez-Urbiola I R, El Bouanani L, Chang J, Avila-Avendano C, Mathews N R, Pintor-Monroy M I and Quevedo-Lopez M 2020 *Adv. Mater. Technol.* **5** 2000534
- [40] Lawrence K, McNamara J and Duncan A 2019 Novel perovskite semiconductors for the detection of special nuclear material *Technical Report SRNL-STI-2019-00592*, 1569632
- [41] Okuno Y, Matsui T, Kobayashi T, Imaizumi M, Jimba Y, Hao Y, Kondo S, Kaneko Y and Kasada R 2022 *ACS Appl. Electron. Mater.* **4** 3411–20
- [42] Krishnan N and Srinivasan S 2020 Scalable low-cost large-area micro-structured thermal neutron detectors *Thesis* (available at: <https://hdl.handle.net/10735.1/9167>)
- [43] Fontana C L, Lunardon M, Pino F E, Stevanato L, Carnera A, Sada C, Soramel F and Moretto S 2017 A distributed data acquisition system for signal digitizers with on-line analysis capabilities 2017 *IEEE Nuclear Science Symp. and Medical Imaging Conf. (NSS/MIC)* (IEEE) pp 1–5
- [44] Fontana C L, Carnera A, Lunardon M, Pino F E, Sada C, Soramel F, Stevanato L and Moretto S 2018 *Int. J. Mod. Phys. Conf. Ser.* **48** 1860118
- [45] Cesaria M, Mazzeo M, Quarta G, Aziz M R, Nobile C, Carallo S, Martino M, Calcagnile L and Caricato A P 2021 *Nanomaterials* **11** 3210
- [46] Nikl M, Mihokova E, Nitsch K, Somma F, Giampaolo C, Pazzi G, Fabeni P and Zazubovich S 1999 *Chem. Phys. Lett.* **306** 280–4
- [47] Jing Q, Xu Y, Su Y, Xing X and Lu Z 2019 *Nanoscale* **11** 1784–9
- [48] Lu Y, Han Q, Zhao Y, Xie D, Wei J, Yuan P, Yang C, Li Y, Liu X and Gao Y 2020 *Results Phys.* **17** 103087
- [49] Di Girolamo D, Dar M I, Dini D, Gontrani L, Caminiti R, Mattoni A, Graetzel M and Meloni S 2019 *J. Mater. Chem. A* **7** 12292–302
- [50] Li J, Shan X, Bade S G R, Geske T, Jiang Q, Yang X and Yu Z 2016 *J. Phys. Chem. Lett.* **7** 4059–66
- [51] Kondo S, Amaya K and Saito T 2002 *J. Phys.: Condens. Matter* **14** 2093–9
- [52] Yantara N, Bhaumik S, Yan F, Sabba D, Dewi H A, Mathews N, Boix P P, Demir H V and Mhaisalkar S 2015 *J. Phys. Chem. Lett.* **6** 4360–4
- [53] Akkerman Q A, D’Innocenzo V, Accornero S, Scarpellini A, Petrozza A, Prato M and Manna L 2015 *J. Am. Chem. Soc.* **137** 10276–81
- [54] Wang Y, Ren Y, Zhang S, Wu J, Song J, Li X, Xu J, Sow C H, Zeng H and Sun H 2018 *Commun. Phys.* **1** 96
- [55] Brenes R et al 2017 *Joule* **1** 155–67
- [56] Howard J M, Tennyson E M, Barik S, Szostak R, Waks E, Toney M F, Nogueira A F, Neves B R A and Leite M S 2018 *J. Phys. Chem. Lett.* **9** 3463–9